

Scalable Bayesian Divergence Time Estimation With Ratio Transformations

XIANG JI^{1,*}, ALEXANDER A. FISHER², SHUO SU³, JEFFREY L. THORNE^{4,5,6}, BARNEY POTTER⁷,
PHILIPPE LEMEY⁷, GUY BAELE⁷ AND MARC A. SUCHARD^{8,9,10,*}

¹Department of Mathematics, School of Science & Engineering, Tulane University, 6823 St. Charles Avenue, New Orleans, LA 70118, USA

²Department of Statistical Science, Duke University, 214 Old Chemistry, Durham, NC 27708, USA

³MOE International Joint Collaborative Research Laboratory for Animal Health & Food Safety, Jiangsu Engineering Laboratory of Animal Immunology, Institute of Immunology, College of Veterinary Medicine, Nanjing Agricultural University, No. 1 Weigang, Xiaolingwei District, Nanjing, Jiangsu 210095, China

⁴Bioinformatics Research Center, North Carolina State University, Raleigh, NC, USA

⁵Department of Statistics, North Carolina State University, Raleigh, NC, USA

⁶Department of Biological Sciences, North Carolina State University, Ricks Hall, 1 Lampe Dr, Raleigh, NC 27607, USA

⁷Department of Microbiology, Immunology and Transplantation, Rega Institute, Herestraat 49, 3000 Leuven, Belgium

⁸Department of Biomathematics, David Geffen School of Medicine, University of California Los Angeles, Los Angeles, CA, USA

⁹Department of Human Genetics, David Geffen School of Medicine, University of California Los Angeles, Los Angeles, CA, USA

¹⁰Department of Biostatistics, Fielding School of Public Health, University of California Los Angeles, 695 Charles E Young Dr S, Los Angeles, CA 90095, USA

*Correspondence to be sent to: Xiang Ji, Department of Mathematics, School of Science & Engineering, Tulane University, 6823 St. Charles Avenue, New Orleans, LA 70118, USA; E-mail: xji4@tulane.edu; Marc A. Suchard, Department of Human Genetics, David Geffen School of Medicine, University of California Los Angeles, 695 Charles E Young Dr S, Los Angeles, CA 90095; E-mail: msuchard@ucla.edu

Received 02 January 2022; reviews returned 13 June 2023; accepted 30 June 2023

Associate Editor: Ziheng Yang

Abstract.—Divergence time estimation is crucial to provide temporal signals for dating biologically important events from species divergence to viral transmissions in space and time. With the advent of high-throughput sequencing, recent Bayesian phylogenetic studies have analyzed hundreds to thousands of sequences. Such large-scale analyses challenge divergence time reconstruction by requiring inference on highly correlated internal node heights that often become computationally infeasible. To overcome this limitation, we explore a ratio transformation that maps the original $N - 1$ internal node heights into a space of one height parameter and $N - 2$ ratio parameters. To make the analyses scalable, we develop a collection of linear-time algorithms to compute the gradient and Jacobian-associated terms of the log-likelihood with respect to these ratios. We then apply Hamiltonian Monte Carlo sampling with the ratio transform in a Bayesian framework to learn the divergence times in 4 pathogenic viruses (West Nile virus, rabies virus, Lassa virus, and Ebola virus) and the coralline red algae. Our method both resolves a mixing issue in the West Nile virus example and improves inference efficiency by at least 5-fold for the Lassa and rabies virus examples as well as for the algae example. Our method now also makes it computationally feasible to incorporate mixed-effects molecular clock models for the Ebola virus example, confirms the findings from the original study, and reveals clearer multimodal distributions of the divergence times of some clades of interest. [Bayesian inference; divergence time estimation; effective sample size; Hamiltonian Monte Carlo; pathogens; phylogenetics; ratio transformation.]

Since [Zuckerlandl and Pauling \(1962\)](#) proposed the first molecular clock model, the development of more reliable divergence time estimation techniques has thrived. Because evolutionary rate and time are confounded in stochastic models for molecular sequence data, one may improve divergence time inference either via advances in treatment of rates or treatment of times. However, the majority of the effort has centered upon improving the model aspects that describe either how evolutionary rates change across the tree or how divergence events happen on the tree resulting as the positions of internal nodes (e.g., coalescent events and/or birth–death events) while improvement of the estimation machinery has received less attention.

This imbalance is partly due to the constraints on the node heights imposed by the tree structure. Assuming a rooted tree with the root node on the top and tip nodes

at the bottom, an internal node must be higher than its descendant nodes but lower than its parent node. These constraints pose great challenge for inferring internal node heights jointly, so one typically samples or optimizes the height of one node at a time.

Despite this inference difficulty, divergence time estimation is crucial to provide temporal signals for dating biologically important events, from species divergence to viral transmissions in space and time ([Erwin et al. 2011](#); [Meredith et al. 2011](#); [Düx et al. 2020](#); [Lemey et al. 2020](#)). Repeated breakthroughs in sequencing technologies have led to molecular data accumulating at an ever-increasing pace. This often results in data sets that contain so many sequences that the desired divergence time analyses become computationally infeasible. When faced with such obstacles, investigators resort to analyzing only a small proportion of the available data and/or

sacrificing statistical rigor and biological plausibility by adopting procedures and models that are flawed but computationally convenient (see, e.g., [Simion et al. \(2020\)](#)). There is, therefore, substantial value in reducing the amount of computation necessary for statistically sound divergence time inference.

In [Kishino et al. \(2001\)](#), the authors transform the internal node heights of a phylogeny with contemporaneous data (sampled at the same time) into a collection of ratios that sum to 1. With a Dirichlet prior distribution, [Kishino et al.](#) were then able to jointly sample all proportions at one time. Inspired by their pioneering work, we explore a more general ratio transformation, similar to that used in [Fourment and Darling \(2019\)](#), for the internal node heights that one can apply to both serially sampled or contemporaneous data. The ratio transformation serves as a reparameterization that works with any existing phylogenetic models without the need for any specific prior. In fact, the proposed ratio transformation preserves the topology-imposed constraints by its construction, allowing the ratios to be independent so that they are easy to sample from or optimize on.

We here show that one can calculate the transformation and the determinant of the Jacobian matrix of the transformation in linear-time with respect to the number of tips (N). With the determinant of the Jacobian matrix, one can set up the phylogenetic model with respect to the untransformed node heights, but sample from the transformed ratio space. To make use of an advanced linear-time gradient of the log-likelihood algorithm ([Ji et al. 2020](#)), we show that one can transform the gradient with respect to the untransformed node heights to the gradient with respect to the transformed ratio space with $\mathcal{O}(N)$ calculations. The linear-time gradient transformation enables the application of gradient-based Monte Carlo samplers such as the Hamiltonian Monte Carlo (HMC) method ([Neal 2011](#)) in the Bayesian framework. HMC shows great potential for improving computational efficiency in many phylogenetic applications ([Dinh et al. 2017](#); [Ji et al. 2020](#); [Baele et al. 2020](#)).

We apply the ratio transformation to simultaneously learn the branch-specific evolutionary rates and the internal node heights of 4 viral examples with serially sampled data and an algae example with contemporaneous samples and fossil-informed calibration priors. Our method significantly improves inference efficiency with a 5- to 8-fold computational performance increase for our Lassa and rabies virus examples and an 11-fold increase for the algae example. More interestingly, the West Nile virus example shows that our sampler better approximates the posterior density than do classic univariable samplers that suffer from Markov chain Monte Carlo (MCMC) mixing issues. For an Ebola virus example, we show that our method makes it computationally feasible to employ a mixed-effects relaxed clock model ([Bletsa et al. 2019](#)) to account for both clade- and branch-specific effects that reveal clearer multi-modal distribution of divergence times for clades of interest.

MATERIALS AND METHODS

New Approach

In this section, we define necessary notation and derive the ratio transformation and its related linear-time algorithms.

Notation.—Assume the root node is on the top of a rooted phylogeny with N tips and $N - 1$ internal nodes. We use numbers $1, 2, \dots, N$ to denote the tip nodes and numbers $N + 1, N + 2, \dots, 2N - 1$ for the internal nodes where the root node is always $2N - 1$. We use notation $\text{pa}(i)$ to denote the parent node of node i . We denote a branch on the tree by the number of the child node it ends at (i.e., branch i connects node $\text{pa}(i)$ to i). We denote the height (i.e., time) of node i with t_i . When i is a tip node (i.e., $i \in \{1, 2, \dots, N\}$), its height is the sampling time. In divergence time estimation, one is interested in estimating the heights of internal nodes.

Without loss of generality, we derive the ratio transformation where the tip nodes can be associated with serially sampled data and where the transformation with contemporaneous data is then a special case where all tip node times are identical. We first define epochs such that any internal node belongs to one and only one epoch. We then define a ratio parameter ascribed to each of the internal nodes except for the root.

Epoch construction and the ratio transformation.—For an internal node, we refer to its earliest (i.e., highest) descendant tip node as its *anchor node*. Therefore, the anchor node of an internal node is its closest descendant tip node. To make the anchor nodes consistent and unique, we assign an arbitrary ordering among tip nodes to distinguish those with the same sampling times. For example, we pick the tip node with the smallest node number as the anchor node from all closest tip nodes sampled at the same time. We group all internal nodes with the same anchor node into an epoch. We refer to an epoch by the number of its anchor node. An epoch is constructed to have a chain structure from its anchor node up to the highest node in the epoch (see [Fig. 1a](#)). Except for the epoch to which the root node belongs, we refer to the parent node of the highest node in an epoch as its *connecting node* such that the connecting node of an epoch belongs to another epoch. We treat the root node as the connecting node for epochs of its immediate descendant nodes.

Let t_i denote the height of node i and $\mathcal{E}(i)$ be the epoch to which node i belongs. We refer to the epoch to which the root node belongs as the starting epoch and assign it as $\mathcal{E}(2N - 1)$. We abuse notation by referring to the j th node of epoch k as k_j . For epoch k that contains m_k internal nodes with strictly positive branch lengths, we have $\{t_{k_1}, t_{k_2}, \dots, t_{k_{m_k}} : t_{k_1} > t_{k_2} > \dots > t_{k_{m_k}} > t_k\}$. We refer to the connecting node of an epoch as the 0th node of an epoch (i.e., $k_0 = \text{pa}(k_1)$). We define $L_k = t_{k_0} - t_k$ as the length of epoch k (see [Fig. 1b](#)). For the i th internal

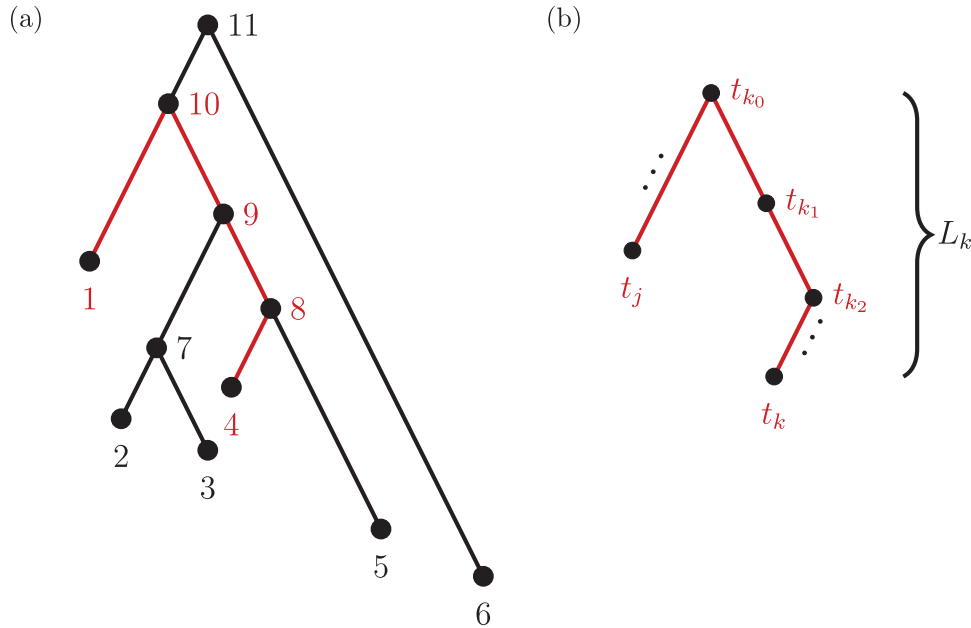


FIGURE 1. Epoch construction on a 6-taxa tree. a) Example tree with serially sampled data. b) One epoch example where epoch k starts from node k_1 down to its anchor node k and node k_0 is the connecting node of epoch k that belongs to epoch j . For the example tree in a) with anchor tip 4, $k = 4$, $j = 1$, and $k_0 = 10$. For anchor tip 2, $k = 2$, $j = 4$, and $k_0 = 9$. For anchor tip 1, $k = 1$ is the starting epoch that contains the root node. Tip nodes 3, 5, and 6 do not anchor any epochs (i.e., their parent nodes belong to epochs anchored at other tip nodes).

node k_i from epoch k (i.e., $i > 0$), we define its ratio parameter r_{k_i} as

$$r_{k_i} = \frac{t_{k_i} - t_k}{t_{k_{i-1}} - t_k}, \tag{1}$$

where t_k is the height of the anchor node of epoch k and $k_{i-1} = \text{pa}(k_i)$. Note that the anchor node of epoch k is not necessarily immediately descendant to node k_i , whereas node k_i is always immediately descendant to node k_{i-1} . In fact, the anchor node of epoch k is the highest descendant tip node for all nodes in the epoch (by definition) and is only immediately descendant to the last node k_{m_k} of the epoch. Therefore, when $i \neq 1$, node k_{i-1} and node k_i are both from epoch k . And when $i = 1$, node k_0 is the connecting node of epoch k that belongs to another epoch and the denominator in Equation (1) becomes L_k (i.e., the length of epoch k). One can write the time of an internal node as a function of the ratios and the epoch lengths as

$$t_{k_i} = L_k \prod_{n=1}^i r_{k_n} + t_k. \tag{2}$$

To ease notation, let $S_{k_i} = \prod_{n=1}^i r_{k_n}$ be the product of ratios for internal node k_i of epoch k . Equation (2) simplifies to

$$t_{k_i} = L_k S_{k_i} + t_k. \tag{3}$$

Interestingly, there is only one degree of freedom for all epoch lengths because

$$\begin{aligned} t_{k_0} &= t_k + L_k \\ &= t_{\mathcal{E}(k_0)} + L_{\mathcal{E}(k_0)} S_{k_0}, \end{aligned} \tag{4}$$

such that the length of epoch k is determined by the length of the epoch of its connecting node (k_0) and the two associated anchor node times ($t_k, t_{\mathcal{E}(k_0)}$). We arrive at the following recursive relationship for epoch lengths

$$L_k = t_{\mathcal{E}(k_0)} - t_k + L_{\mathcal{E}(k_0)} S_{k_0}. \tag{5}$$

Therefore, there is effectively only one degree of freedom for the scale of time with all ratios denoting the relative height an internal node has using its parent node and the anchor node as reference. There are many choices for modeling this single dimension for time scale (e.g., one may arbitrarily choose one of the epoch lengths). We pick the starting epoch length as the free parameter $L_{\mathcal{E}(2N-1)} = t_{2N-1} - t_{\mathcal{E}(2N-1)}$, which we refer to as the *height parameter* because it represents the height difference from the root node to its closest tip node (all tip nodes are descendants of the root) and is the only dimension. We refer to the space of the height and $N - 2$ ratio parameters as the *ratio space*. We refer to the space of all untransformed internal node heights as the *height space*. We refer to the transformation from the height space into the ratio space as the *ratio transform*.

Algorithm 1 illustrates the ratio transform through a single post-order traversal that visits every node on

Algorithm 1 Ratio transform through a single post-order traversal

for node i in a post-order traversal **do**
 if i is a tip node **then**
 Set the anchor tip of epoch i as node i .
 else
 Set the anchor tip of i the same as the highest anchor tip of its immediate descendant nodes.
 Calculate $r_i = \frac{t_i - t_{\mathcal{E}(i)}}{t_{\text{pa}(i)} - t_{\mathcal{E}(i)}}$ according to Equation (1).
 end if
end for

the tree in a descendant-first manner. Likewise, one can perform the inverse ratio transform to get node heights from the ratios by reversing Equation (1) through a pre-order traversal.

Gradient and Jacobian.—Many modern inference machineries benefit from gradient information to find descending directions of the likelihood surface or to efficiently integrate dynamics along the surface for generating Monte Carlo proposals (e.g., Ji et al. (2020) contains gradient applications in non-linear optimization and Bayesian posterior sampling). When transforming probability densities from their original space into another (e.g., the ratio space in this case), one needs the determinant of the Jacobian matrix to correctly “weight” the transformed density (see Theorem 2.1.5 from Casella and Berger (2001)). In this section, we derive algorithms for transforming the “unweighted” likelihood into the ratio space together with the associated quantities from the log-determinant of the Jacobian matrix to correctly set the “weight.”

In Ji et al. (2020), we introduced a linear-time algorithm for calculating the gradient of the log-likelihood with respect to the branch length $b_i = \tau_i(t_i - t_{\text{pa}(i)})$ that is the product of the evolutionary rate τ_i and the time duration $t_i - t_{\text{pa}(i)}$ of branch i . To calculate the gradient with respect to node heights, one starts with the gradient with respect to branch lengths and finishes via the chain rule. More specifically, for node h with its two immediate descendant nodes i and j , the derivative of the log-likelihood, $\log \mathbb{P}(\mathbf{Y})$, with respect to t_h is:

$$\begin{aligned} & \frac{\partial}{\partial t_h} \log \mathbb{P}(\mathbf{Y}) \\ &= \begin{cases} \frac{\partial \log \mathbb{P}(\mathbf{Y})}{\partial b_h} \frac{\partial b_h}{\partial t_h} + \frac{\partial \log \mathbb{P}(\mathbf{Y})}{\partial b_j} \frac{\partial b_j}{\partial t_h} + \frac{\partial \log \mathbb{P}(\mathbf{Y})}{\partial b_i} \frac{\partial b_i}{\partial t_h}, & h \neq 2N - 1 \\ \frac{\partial \log \mathbb{P}(\mathbf{Y})}{\partial b_i} \frac{\partial b_i}{\partial t_h} + \frac{\partial \log \mathbb{P}(\mathbf{Y})}{\partial b_j} \frac{\partial b_j}{\partial t_h}, & h = 2N - 1. \end{cases} \end{aligned} \quad (6)$$

It is important to recall that a ratio parameter is only explicit to the node it assigns to and all its descendant nodes by Equation (2). Therefore, we only need

the partial derivatives $\partial t_k / \partial r_h$ from node h and all its descendant nodes k to finish the chain rule

$$\frac{\partial}{\partial r_h} \log \mathbb{P}(\mathbf{Y}) = \sum_k \left[\frac{\partial}{\partial t_k} \log \mathbb{P}(\mathbf{Y}) \frac{\partial t_k}{\partial r_h} \right]. \quad (7)$$

To derive the partial derivative $\partial t_k / \partial r_h$ for any two nodes h and k such that node k is a descendant of node h , we separate the node pairs into two cases. The first case considers node h and node k in the same epoch (including the pair where $h = k$, e.g., Equation (3)), such that

$$\begin{aligned} \frac{\partial t_k}{\partial r_h} &= L_{\mathcal{E}(k)} \frac{\partial S_k}{\partial r_h} \\ &= \frac{t_k - t_{\mathcal{E}(k)}}{r_h}. \end{aligned} \quad (8)$$

For the other case where node h and node k belong to different epochs, we start with revealing the relationship between the partial derivatives of node k 's height t_k and its connecting node $\mathcal{E}(k)_0$'s height $t_{\mathcal{E}(k)_0}$ with respect to the same ratio r_h (e.g., plug Equation (5) in Equation (3)), such that

$$\begin{aligned} \frac{\partial t_k}{\partial r_h} &= S_k \frac{\partial (t_{\mathcal{E}(k)_0} - t_{\mathcal{E}(k)} + L_{\mathcal{E}(k)_0} S_{\mathcal{E}(k)_0})}{\partial r_h} \\ &= S_k \frac{\partial t_{\mathcal{E}(k)_0}}{\partial r_h}. \end{aligned} \quad (9)$$

Equation (9) shows that one obtains the partial derivative of a node height t_k with respect to ratio r_h by multiplying the related ratio product (i.e., S_k) and the partial derivative of the node height $t_{\mathcal{E}(k)_0}$ with respect to ratio r_h (i.e., $\partial t_{\mathcal{E}(k)_0} / \partial r_h$). Combining Equations (8) and (9), we inductively derive a general expression for the derivatives where node h and node k do not belong to the same epoch. We arrive at this derivation through the existence of a series of connecting nodes (when traveling from node k to node h) starting from epoch $\mathcal{E}(k)$ that the last connecting node belongs to the same epoch as node h , that is, $\mathcal{E}(\mathcal{E}(\dots \mathcal{E}(k)_0)_0) = \mathcal{E}(h)$. The general expression for the derivative becomes

$$\frac{\partial t_k}{\partial r_h} = S_k S_{\mathcal{E}(k)_0} \dots S_{\mathcal{E}(\dots \mathcal{E}(k)_0)_0} \frac{\partial t_{\mathcal{E}(\dots \mathcal{E}(k)_0)_0}}{\partial r_h}. \quad (10)$$

By naively plugging Equations (8) and (10) into Equation (7), we obtain the gradient with respect to the ratio space. However, this operation amounts to $\mathcal{O}(N^2)$ computations for transforming the gradient. To overcome this computational burden, we develop a linear-time $\mathcal{O}(N)$ algorithm for transforming the gradient.

Post-order traversal Consider 3 internal nodes h , i , and j such that node h is the parent node of node i and node j . The linear-time algorithm for transforming the gradient with respect to ratio parameters builds on 2 properties of the ratio transformation. The first property is that any

descendant node of node h except node i or node j is a descendant node of either node i or node j (for bifurcating trees). The other property is that node h belongs to the same epoch as either node i or node j . As is common in dynamic programming algorithms, we want to derive the relationship of $\partial t_k / \partial r_h$ with $\partial t_k / \partial r_i$ and $\partial t_k / \partial r_j$, where node k is descendant of node h to reuse quantities cached from evaluating Equation (7) on descendant nodes. More specifically, we want to reuse the summations already determined for $(\partial / \partial r_i) \log \mathbb{P}(\mathbf{Y})$ and $(\partial / \partial r_j) \log \mathbb{P}(\mathbf{Y})$ when calculating $(\partial / \partial r_h) \log \mathbb{P}(\mathbf{Y})$ as in Equation (9).

Without loss of generality, we assume node h belongs to the same epoch as node i . The following relationships between derivatives with respect to the three ratio parameters r_h , r_i , and r_j enable the linear-time algorithm through a single post-order traversal to update the gradient from the height space into the ratio space (except for the height parameter). From Equation (8) and Equation (10), when node k is a descendant of node i (including $i = k$) such that node h and node k are in the same epoch,

$$\frac{\partial t_k}{\partial r_h} = \frac{\partial t_k}{\partial r_i} \frac{r_i}{r_h}. \quad (11)$$

When node k is descendant of node j (including $j = k$) such that node h is the connecting node to the epoch $\mathcal{E}(j)$ where node j is the first node,

$$\frac{\partial t_k}{\partial r_h} = \frac{\partial t_k}{\partial r_j} \frac{r_j}{L_{\mathcal{E}(j)}} \frac{\partial t_h}{\partial r_h}. \quad (12)$$

Note that we model the ratio parameters as independent of each other (i.e., $\partial r_h / \partial r_i = \partial r_h / \partial r_j = 0$). Equations (11) and (12) come from the special structure of the transform that the height of an internal node is a product of a series of ratio parameters with one single height parameter. Algorithm 2 illustrates updating the gradient with respect to all ratio parameters (except for the height parameter) where one reuses the derivatives of the log-likelihood with respect to two immediate descendant nodes (i.e., nodes i and j) to calculate the derivative of the log-likelihood with respect to the parent node (i.e., node h).

Pre-order traversal We now update the gradient of the log-likelihood with respect to the height parameter which is the only dimension left in the ratio transform. We use a pre-order traversal to update the gradient in this dimension because the transformation of all internal node heights depends on it. The update is

$$\frac{\partial}{\partial L_{\mathcal{E}(2N-1)}} \log \mathbb{P}(\mathbf{Y}) = \sum_k \left[\frac{\partial}{\partial t_k} \log \mathbb{P}(\mathbf{Y}) \frac{\partial t_k}{\partial L_{\mathcal{E}(2N-1)}} \right]. \quad (13)$$

Based on Equation (4), we calculate all the partial derivatives $\partial t_k / \partial L_{\mathcal{E}(2N-1)}$ according to Algorithm 3 through a single pre-order traversal.

Algorithm 2 Transforming the gradient of the log-likelihood with respect to ratio parameters by post-order traversal

for node h in a post-order traversal **do**

if h is a tip node **then**

 Set the gradient of h as 0.

else

 Let node i and node j be the two immediate descendant nodes of node h such that node i and node h belong to the same epoch.

 Set the gradient of h as

$$\frac{\partial}{\partial r_h} \log \mathbb{P}(\mathbf{Y}) = \frac{\partial}{\partial r_i} \log \mathbb{P}(\mathbf{Y}) \frac{r_i}{r_h} + \frac{\partial}{\partial r_j} \log \mathbb{P}(\mathbf{Y}) \frac{r_j}{L_{\mathcal{E}(j)}} \frac{\partial t_h}{\partial r_h} + \frac{\partial}{\partial t_h} \log \mathbb{P}(\mathbf{Y}) \frac{\partial t_h}{\partial r_h}.$$

end if

end for

Algorithm 3 Transforming gradient of the log-likelihood with respect to the height parameter by pre-order traversal

for node k in a pre-order traversal **do**

if k is the root node **then**

 Set the derivative of node height k with respect to height parameter as 1 (i.e., $\frac{\partial t_{2N-1}}{\partial L_{\mathcal{E}(2N-1)}} = 1$).

else

 Set the derivative of k as the product of r_k and the derivative of its parent node with respect to height parameter (i.e., $\frac{\partial t_k}{\partial L_{\mathcal{E}(2N-1)}} = r_k \frac{\partial t_{\text{pa}(k)}}{\partial L_{\mathcal{E}(2N-1)}}$).

end if

end for

Determinant of the Jacobian matrix We now derive the Jacobian matrix associated with the ratio transform whose determinant sets the weight for the transformed density. One derives the full Jacobian matrix for the ratio transform by applying Equation (8) and Equation (10). Note the special structure that has $\partial t_k / \partial r_i \neq 0$ if and only if $i = k$ or node k is descendant of node i , and also note the independence between the height parameter and the ratio parameters. By ordering the entries in a descendant node first fashion that coincides with how nodes are visited in a post-order traversal, the Jacobian matrix becomes triangular (including the height parameter). Because the determinant of a triangular matrix only involves the diagonal entries, the determinant of the Jacobian matrix \mathbb{J} becomes

$$\begin{aligned} |\mathbb{J}| &= \prod_i \frac{\partial t_i}{\partial r_i} \\ &= \prod_i [t_{\text{pa}(i)} - t_{\mathcal{E}(i)}]. \end{aligned} \quad (14)$$

Algorithm 4 Calculating gradient of the log-determinant of the Jacobian matrix with respect to ratio parameters by post-order traversal

```

for node  $k$  in a post-order traversal do
  if  $k$  is a tip node then
     $\frac{\partial}{\partial r_k} \log |\mathbf{J}| = 0$ 
  else
    Let node  $i$  and node  $j$  be the two immediate descendant nodes of node  $k$  such that node  $i$  and node  $k$  belong to the same epoch, and compute
     $\frac{\partial}{\partial r_k} \log |\mathbf{J}| = \frac{\partial}{\partial r_i} \log |\mathbf{J}| \frac{r_i}{r_k} + \frac{\partial}{\partial r_j} \log |\mathbf{J}| \frac{r_j}{L_{\mathcal{E}(j)}} \frac{\partial t_k}{\partial r_k} + \frac{1}{t_k - t_{\mathcal{E}(k)}} \frac{\partial t_k}{\partial r_k}$ 
    end if
  end for
for every internal node  $k$  do
  Update  $\frac{\partial}{\partial r_k} \log |\mathbf{J}| = \frac{\partial}{\partial r_k} \log |\mathbf{J}| - \frac{1}{r_k}$ 
end for

```

Gradient of log-determinant of the Jacobian matrix We complete this section with a final linear-time algorithm for calculating the gradient of the log-determinant of the Jacobian matrix with respect to the ratio space for applying HMC on this transformed space as described in the next section. This additional gradient component facilitates using HMC to sample all dimensions jointly in the ratio space. Similar to the case of updating the gradient of the log-likelihood from the original space into the ratio space, naively applying Equation (8) and Equation (10) results in an undesired quadratic computational load. One can benefit from the same properties that lead to Algorithm 2 with a modified two-pass linear-time Algorithm 4 that calculates all the derivatives of the log-determinant of the Jacobian matrix with respect to the ratio parameters.

Hamiltonian Monte Carlo.—HMC is a state-of-the-art MCMC method that generates efficient proposals through Hamiltonian dynamics (Neal 2011) for the Metropolis–Hastings algorithm (Metropolis et al. 1953; Hastings 1970). For an arbitrary and unbounded parameter of interest θ with the posterior density $\pi(\theta)$, HMC introduces an auxiliary parameter \mathbf{p} and samples from the product density $\pi(\theta, \mathbf{p}) = \pi(\theta)\pi(\mathbf{p})$ through:

$$\begin{aligned} \frac{d\mathbf{p}}{dt} &= -\nabla U(\theta) = \nabla \log \pi(\theta) \text{ and} \\ \frac{d\theta}{dt} &= \nabla K(\mathbf{p}) = \mathbf{M}^{-1}\mathbf{p}, \end{aligned} \quad (15)$$

where $U(\theta)$ is the “potential energy” often set to the negative log-posterior density and $K(\mathbf{p}) = \mathbf{p}'\mathbf{M}^{-1}\mathbf{p}/2$ is the “kinetic energy” as the auxiliary parameter \mathbf{p} typically follows a multivariate normal distribution $\mathbf{p} \sim \mathcal{N}(\mathbf{0}, \mathbf{M})$ with a “mass matrix” \mathbf{M} as the covariance matrix. HMC has shown great potential in diverse

phylogenetic applications (Dinh et al. 2017; Baele et al. 2020; Ji et al. 2020).

Naive application of HMC on the space of internal node heights is highly inefficient because of the irregular constraints on these parameters. Instead, the ratio space is trivial to extend such that it is unbounded by applying a logit-transform to each ratio independently and a log-transform to the single height parameter. We apply HMC on the (extended) ratio space for efficient sampling of all internal node heights while fixing the tree topology and other model parameters. Finally, we also apply HMC for jointly sampling the evolutionary rates and times (i.e., divergence time estimation) and explore the additional efficiency gain this affords.

Preconditioning with adaptive variance The geometric structure of the posterior distribution significantly affects the computational efficiency of HMC. For example, when the scales of the posterior distribution vary among individual parameters, failing to account for such structure may reduce the efficiency of HMC (Neal 2011; Stan Development Team 2017; Ji et al. 2020). We can adapt HMC for such structure by modifying the dynamics in Equation (15) via an appropriately chosen mass matrix \mathbf{M} . In Ji et al. (2020), we employ a mass matrix informed by the diagonal entries of the Hessian matrix of the log-posterior to account for the variable scales among dimensions. Unfortunately, one needs the full Hessian matrix in the original height space to transform into the Hessian matrix with respect to the ratio space. This strategy is too computationally expensive to adopt.

To incorporate information from the covariance matrix without excessive computational burden, we seek an alternative adaptive MCMC procedure (Haario et al. 1999; Andrieu and Thoms 2008; Roberts and Rosenthal 2009). Adaptive MCMC has previously found its way into Bayesian phylogenetic inference (Baele et al. 2017) and we use this technique here to tune \mathbf{M} to the covariance matrix estimated from previous samples in the Markov chain. We further restrict \mathbf{M} to remain diagonal and hence to scale the ratio dimensions according to their marginal covariance. This restriction is commonly imposed to regularize the estimate, and a diagonal matrix alone can greatly enhance sampling efficiency of HMC in many situations (Stan Development Team 2017; Ji et al. 2020). We start the HMC sampler with an identity matrix as \mathbf{M} to collect an initial set of samples (e.g., 200 in our analyses), after which we employ the sample covariance to tune \mathbf{M} adaptively. Also, we only update the diagonal mass matrix every 10 HMC iterations so that the cost of computing the adaptive \mathbf{M} diagonals remains negligible.

Data

We examine the molecular evolution of West Nile virus (WNV) in North America (1999–2007), rabies virus (RABV) in the United States (1982–2004), the S segment

of Lassa virus (LASV) in West Africa (2008–2013), Ebolavirus (EBOV) in the Democratic Republic of Congo, Africa (2018–2020), and the coralline red algae subclass *Corallinophycidae* with contemporaneous data and fossil record informed calibration priors on 6 internal nodes (Biek et al. 2007; Pybus et al. 2012; Andersen et al. 2015; Mbala-Kingebeni et al. 2021; Pena et al. 2020). In all data sets, phylogenetic analyses have revealed a high variation of the evolutionary rates across branches in the underlying phylogeny.

West Nile virus West Nile virus is a mosquito-borne RNA virus that involves multiple species of mosquitoes and birds where birds are the primary host. WNV first emerged in the Americas in New York in 1999, and quickly spread across the continent, causing an epidemic of human disease accompanied with massive bird deaths. In total, human infections have resulted in over 48,000 reported cases, 24,000 reported neuroinvasive cases, and over 2300 deaths (Hadfield et al. 2019). The molecular sequence data consist of 104 full genomes, with a total alignment length of 11,029 nucleotides, and were collected from infected human plasma samples from 2003 to 2007 as well as near-complete genomes obtained from GenBank (Pybus et al. 2012).

Rabies virus Rabies is an RNA virus that can cause zoonotic disease and is responsible for over 50,000 human deaths every year. Besides bats, several terrestrial carnivore species such as raccoons are important rabies reservoirs. Before the detection of a raccoon-specific rabies virus variant in 1970s, there was only limited focus on raccoons as a primary host for rabies in the southeastern United States, specifically Florida. Over the following decades, an emergence of the virus spread along the mid-Atlantic coast and northeastern United States. We analyze the molecular sequences originally described in Biek et al. (2007) that previously served as an example dataset in work on the flexible non-parametric skygrid coalescent model (Gill et al. 2016). The data consist of 47 sequences sampled from rabid raccoons between 1982 and 2004 that contain the complete rabies nucleoprotein gene (1365 bp) with part of a noncoding region (87 bp) immediately following its 3' end, and a large portion of the glycoprotein gene (1359 bp).

Lassa virus Lassa virus is the causative agent of Lassa fever, a hemorrhagic fever endemic to parts of West Africa that is responsible for thousands of deaths and tens-of-thousands of hospitalizations each year (Andersen et al. 2015). LASV infections can lead to Lassa fever, a hemorrhagic fever similar to that from EBOV and endemic to parts of West Africa. Despite the fact that Lassa fever can lead to over 50% fatality rates among hospitalized patients, an effective vaccine for LASV has yet to be developed and approved. Unlike EBOV (see next paragraph), which passes directly between humans, LASV circulates in a rodent (*Mastomys natalensis*)

reservoir and mainly infects humans through contact with rodent excreta. The LASV genome is comprised of 2 negative-sense single-stranded RNA segments: the L segment is 7.3 kilobase pairs (kb) long, and the S segment is 3.4 kb long. In this paper, we use the S segment of the LASV sequence data set of Andersen et al. (2015) that consists of 211 samples obtained at clinics in both Sierra Leone and Nigeria, rodents in the field, laboratory isolates and previously sequenced genomes.

Ebola virus The Ebola virus disease (EVD) outbreak in North Kivu province in the Democratic Republic of Congo (DRC) during 2018–2020 was the world's second largest Ebola outbreak on record. It led to 3481 total cases with 2299 deaths (World Health Organization 2021). One patient who received the recombinant vesicular stomatitis virus-based vaccine was diagnosed with EVD and recovered within 14 days after treatment. However, 6 months later, the same patient presented again with severe EVD-like illness and EBOV viremia and died (Mbala-Kingebeni et al. 2021). The molecular sequence data consist of 297 sequenced isolates that contain 72 epidemiologically linked cases to the patient's second infection.

Algae The coralline red algae (*Corallinophycidae*) are characterized by the presence of calcite crystals in their cell walls. Corallines, as a group, possess the richest fossil record among marine algae. In their pioneering study, Pena et al. (2020) use a multi-locus dataset with taxon sampling and comprehensive collection of coralline fossil records to reconstruct a time-calibrated phylogeny of the subclass *Corallinophycidae*. The algae dataset contains 123 *Corallinophycidae* taxa and 9 out-group species with 7 genes (LSU, SSU, 23S, *cos1*, EF2, *psbA*, *rbcL*) concatenated into an alignment of more than 8000 bp. We employ the same fossil-informed normal priors on 6 internal nodes as in the original study (Pena et al. 2020). More specifically, we place the same normal priors on the time to most recent common ancestor (tMRCA) with mean 18.0 Mya (million years ago) and standard deviation 8.40 Mya for clade A: *Harveyolithon*, mean 23.0 Mya and standard deviation 4.65 Mya for clade B: *Porolithon*, mean 26.8 Mya and standard deviation 5.10 Mya for clade C: *Lithophyllum pustulatum*, mean 66.0 Mya and standard deviation 2.23 Mya for clade D: *Hydrolithoideae*, mean 116.66 Mya and standard deviation 0.66 Mya for clade E: *Hapalidiales*, and mean 137.63 Mya and standard deviation 1.23 Mya for clade F: *Sporolithales* as shown in Figure 7.

Mixed-effects Relaxed Clock Model

We employ mixed-effects relaxed clock models (as detailed in Bletsas et al. (2019)) to learn the evolutionary rates of the 4 viral datasets and the algae dataset. More specifically, we use the same random-effects relaxed clock model detailed in Ji et al. (2020) for the analysis of WNV, RABV, and LASV datasets. For the

EBOV example, we use a mixed-effects relaxed clock model with clade-specific fixed-effects to model clade-specific rate variations among the 3 branches leading to 3 clades of interest (relapse clade, MAN14985 clade, and KAT21596 clade). For the algae example, we use a mixed-effects relaxed clock model with clade-specific fixed-effects to model clade-specific rate variations among the 8 clades of interest as in the original study. The use of the clade-specific fixed-effects mimics a local clock model that allows us to model and compare possibly within-clade rate variations but has previously not been computationally feasible.

Priors

We use the same data partitions, substitution models, and prior distributions as in each example's original study (Biek et al. 2007; Pybus et al. 2012; Andersen et al. 2015; Pena et al. 2020; Mbala-Kingebeni et al. 2021).

Implementations

We have implemented the algorithms in this manuscript within the development branch of the software package BEAST (SHA 17da204e2d9bdadb6c8284fd092413054f161bdc) (Suchard et al. 2018) with likelihood computations off-loaded to the high-performance BEAGLE library (SHA 3bdb30bd645e15983f8c8cf952564813e306ad83) (Ayres et al. 2019). We provide instructions and the BEAST XML files for reproducing these analyses on Github at https://github.com/suchard-group/hmc_divergence_time_manuscript_supplement.

RESULTS

We summarize the computational efficiency improvement with HMC on the ratio space followed by our biological findings on divergence time estimations of the 5 examples.

Computational Performance

We infer the posterior distribution of all internal node heights using 2 different MCMC proposal kernels implemented in BEAST (Suchard et al. 2018) with likelihood computations off-loaded to the high-performance BEAGLE library (Ayres et al. 2019). The first kernel proposes new values for one internal node height at a time from their support. This represents the current best-practice approach used in BEAST and we will refer to this kernel as “univariable.” The other proposal kernel utilizes HMC with a diagonal mass matrix informed by adaptive variance on the ratio space that we will refer to as “HMC.” As is conventional for Bayesian phylogenetics, we employ a Metropolis-within-Gibbs (Tierney 1994; Andrieu et al. 2003) approach that cycles between sampling the tree, the evolutionary rates and the other phylogenetic modeling parameters, each from their

respective full conditional distributions (see, e.g., Equation (6) in Hassler et al. (2023) for more details).

As expected, sampling the topology and the high-dimensional rate and time (i.e., node height) parameters is computationally rate-limiting. Therefore, we explore 2 scenarios: 1) we sample divergence times only, while keeping the evolutionary rate and all other parameters fixed in scenario “time”; and 2) we sample evolutionary rate and time jointly, while keeping all other parameters fixed in scenario “rate & time.” We compare the efficiency of these proposal kernels through their effective sample size (ESS) per unit time for divergence time estimations. For each analysis, we run the MCMC iterations with each of the kernels for roughly the same run time (more details regarding chain lengths can be found in the supplementary BEAST XML files). This strategy aims to accommodate the difference in computational cost per MCMC iteration among kernels for fair comparisons. To maintain identifiability of internal nodes, we constrain the comparisons of the WNV, RABV, LASV, and algae examples to a fixed topology that was randomly selected from its posterior distribution. Specifically, we set all parameters, except for those of interest in each scenario, fixed to their realized values from a randomly selected MCMC iteration. The topologies and parameter values of the WNV and LASV examples are the same as in Ji et al. (2020). This topology constraint brings no additional work or difficulty for applying our method to integrate over topology space since one typically cycles between sampling the topology, the divergence times and other parameters, each from their respective full conditional distributions as in a Metropolis-within-Gibbs inference strategy (Tierney 1994; Andrieu et al. 2003). To demonstrate, we relax the topology constraint (i.e., we don't fix the tree topology) for the EBOV example. We also relax the topology constraint when inferring the maximum clade credible evolutionary trees for all 5 examples and report posterior estimates for the evolutionary rate parameters in this scenario in the following section. We present the computational efficiency improvement with HMC in the ratio space for sampling node heights. The application of HMC on the ratio dimensions greatly improves the mixing of the MCMC chain, whereas the univariable samplers are problematic for learning the height of some internal nodes that are close to the root in the WNV example.

Figure 2 illustrates the posterior sampling efficiency with HMC and univariable samplers in terms of ESS per unit time. Table 1 shows the summary statistics of the efficiency gain of the HMC sampler compared with the univariable samplers for the 3 examples. We exclude the WNV example from the efficiency comparison because the poor mixing with univariable samplers leads to an inflated speed-up for HMC. The HMC sampler yields at least 5-fold efficiency improvement in terms of the minimum ESS per unit time in the RABV, LASV, and algae examples that have no difficulties of mixing for the univariable sampler.

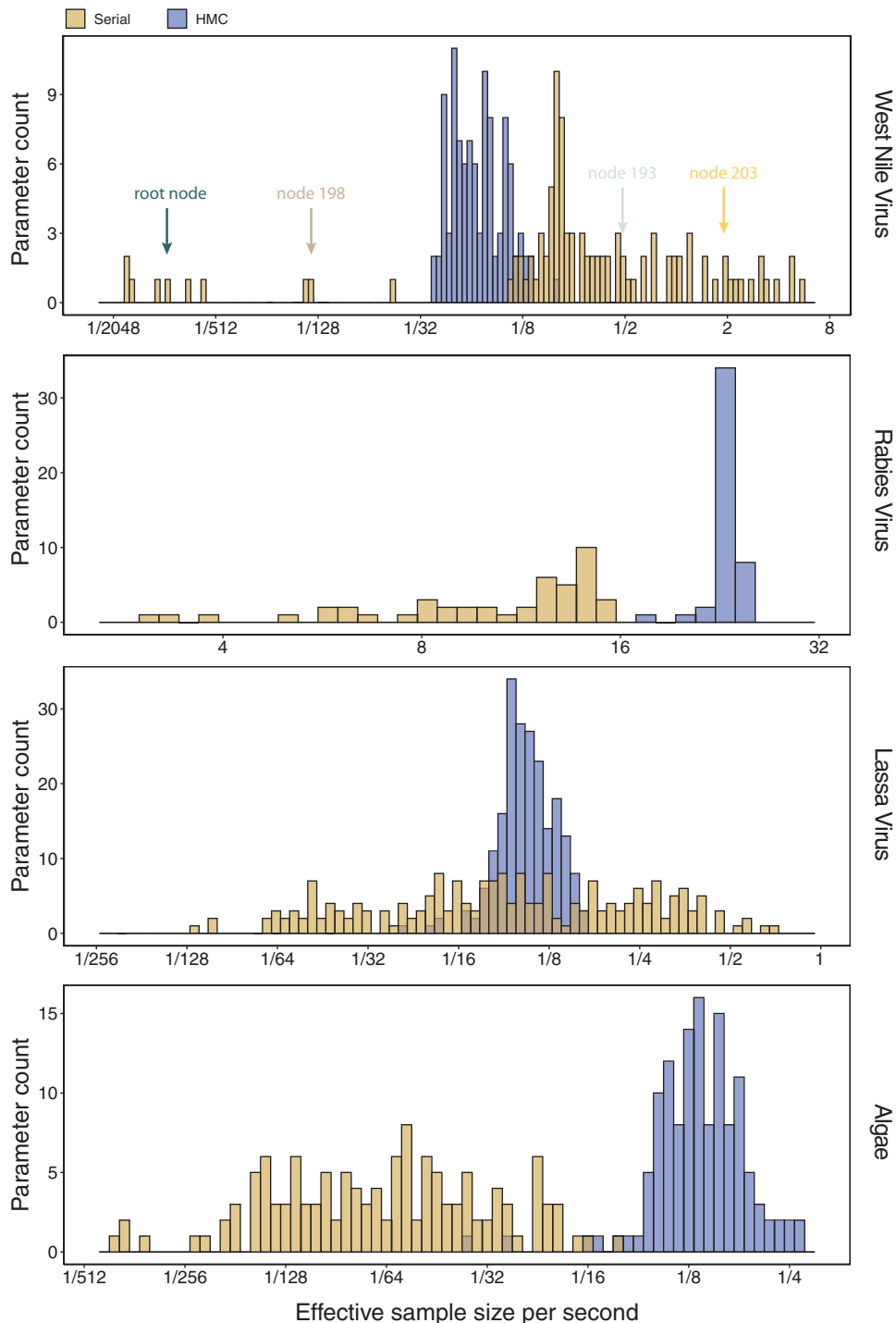


FIGURE 2. Posterior sampling efficiency on all node height parameters for the WNV, RABV, LASV, and algae examples. We bin parameters by their ESS/s values. The 2 proposal kernels employed in the MCMC are color-coded: a univariable proposal kernel and an HMC proposal kernel with an adaptive mass matrix.

Divergence Time Estimations

We summarize divergence time estimation results for each of the five examples.

West Nile virus Our analysis estimates the tree-wise (fixed-effect) rate with posterior mean 5.67 (95% Bayesian credible interval: $5.05, 6.30$) $\times 10^{-4}$ substitutions per site per year and an estimated

TABLE 1 Computational performance of proposal kernels for the RABV, LASV, and algae examples. Computational efficiency measured in terms of effective sample size per second (ESS/s) and effective sample size per proposal (ESS/N). We compare the performance of our HMC proposal kernels operating on the transformed ratio space with a univariable (univariable) proposal kernel on the original node height space. We report speedup with respect to the minimum and median ESS/s and ESS/N (listed in the columns of “univariable” and “HMC”) across parameters for each example and method. We do not report the unreliably high speed-ups for the WNV dataset because of mixing issues under the “univariable” kernel.

Source			Univariable		HMC		Speedup	
			Minimum	Median	Minimum	Median	Minimum	Median
ESS/s	RABV	Time	3.187	12.154	17.358	23.579	5.4×	1.9×
		Rate & Time	0.927	4.638	6.324	8.355	6.8×	1.8×
	LASV	Time	0.008	0.090	0.042	0.104	5.0×	1.2×
		Rate & Time	0.002	0.016	0.018	0.040	8.0×	2.4×
	Algae	Time	2.47E-3	1.59E-2	2.72E-2	1.34E-1	11.0×	8.4×
		Rate & Time	9.01E-5	7.37E-4	1.26E-3	4.26E-3	14.0×	5.8×
ESS/N	RABV	Time	2.12E-4	8.10E-4	3.39E-2	4.60E-2	159.3×	56.7×
		Rate & Time	2.26E-4	1.13E-3	2.45E-2	3.24E-2	108.3×	28.6×
	LASV	Time	8.68E-6	9.45E-5	1.17E-3	2.92E-3	134.8×	30.9×
		Rate & Time	2.70E-6	1.98E-5	1.21E-3	2.63E-3	447.3×	132.9×
	Algae	Time	4.31E-5	2.77E-4	1.60E-3	7.86E-3	37.2×	28.4×
		Rate & Time	2.51E-6	2.05E-5	2.87E-4	9.67E-4	114.2×	47.2×

variability characterized by the scale parameter of the lognormal distributed branch-specific random-effects with posterior mean 0.34 (0.21, 0.47). These values are similar to previous estimates (Pybus et al. 2012; Ji et al. 2020). Figure 3 shows the evolutionary tree explored in the WNV example as well as trace plots of several nodes of interest. Our analysis estimates the date of the epidemic origin to have posterior mean 1998.6(1997.8, 1999.1) similar to previous estimates. Matching previous findings that the American epidemic was likely to originate from the introduction of a single highly pathogenic lineage, our analysis infers the NY99 lineage to be basal to all other genomes.

Of important note, the MCMC chain suffers poor mixing for some height dimensions close to the root (including the root) under the “univariable” kernel as illustrated by the trace plot in Figure 3b I and II. The mixing issue propagates from the root node to a few of its descendant nodes (e.g., node 198) that plagues over these dimensions because univariable samplers propose a new value for an internal node’s height from the interval set by the height of its parent and closest descendant node. Such a tree-like boundary structure requires multiple height changes on an internal node and the nodes setting its boundaries in the same direction before a “big” move is possible that often fails by one of these dimensions moving at the opposite direction.

Rabies virus Our analysis results in a posterior mean rate of 2.12 (1.73, 2.51) $\times 10^{-4}$ substitutions per site per year. The estimated scale parameter has posterior mean 0.10 (0.00, 0.24). Figure 4 shows the maximum clade credible evolutionary tree of the RABV example. Our analysis estimates the date of the root of the tree to be 1971.9 (1951.3, 1979.7). This is slightly older than the estimate in Biek et al. (2007) and our 95% Bayesian credible interval is wider.

Lassa virus Our analysis yields a posterior mean rate of 0.97(0.81, 1.14) $\times 10^{-3}$ substitutions per site per year. The estimated scale parameter has posterior mean 0.089(0.035, 0.140). Figure 5 shows the maximum clade credible evolutionary tree of the LASV example. The date of the root of the tree is inferred to be 1434.0(1059.0, 1601.7). This agrees with the finding by Andersen et al. (2015) that LASV is a long-standing human pathogen whose most recent common ancestor existed around 600 years ago.

Ebolavirus Our analysis yields a posterior mean rate 7.70 (6.63, 8.82) $\times 10^{-4}$ substitutions per site per year. The scale parameter has posterior mean 0.98 (0.64, 1.33). Figure 6 shows the maximum clade credible evolutionary tree of the EBOV example. The inferred MCC tree shows a significant slow-down in evolutionary rate on the branch leading to the relapse clade with a posterior mean of 1.95 (0.12, 4.61) $\times 10^{-4}$ substitutions per site per year that roughly spans over 5.3 months, similar to the discovery from Mbala-Kingebeni et al. (2021). The posterior mean branch-specific rate of the two branches leading to the MAN4194 and KAT21596 clades are 5.98 (1.92, 10.84) $\times 10^{-4}$ and 6.30 (0.34, 16.06) $\times 10^{-4}$ substitutions per site per year respectively (please see section for more comparisons between the mixed-effects model and the model employed in the original study). However, our results have more variability in evolutionary rates compared to the original study. The MAN4194 sequence that was collected from the individual with the relapsed Ebola infection is basal to all other DRC sequences within the relapse clade. We estimate the date of the most recent common ancestor (MRCA) of the relapse clade (Fig. 6b II) to be 2019.85 (2019.77, 2019.91). This is similar to the estimate of Mbala-Kingebeni et al. (2021), but our analysis revealed a clearer bimodal posterior distribution that was previously missed. To confirm that the bimodal posterior distribution was not

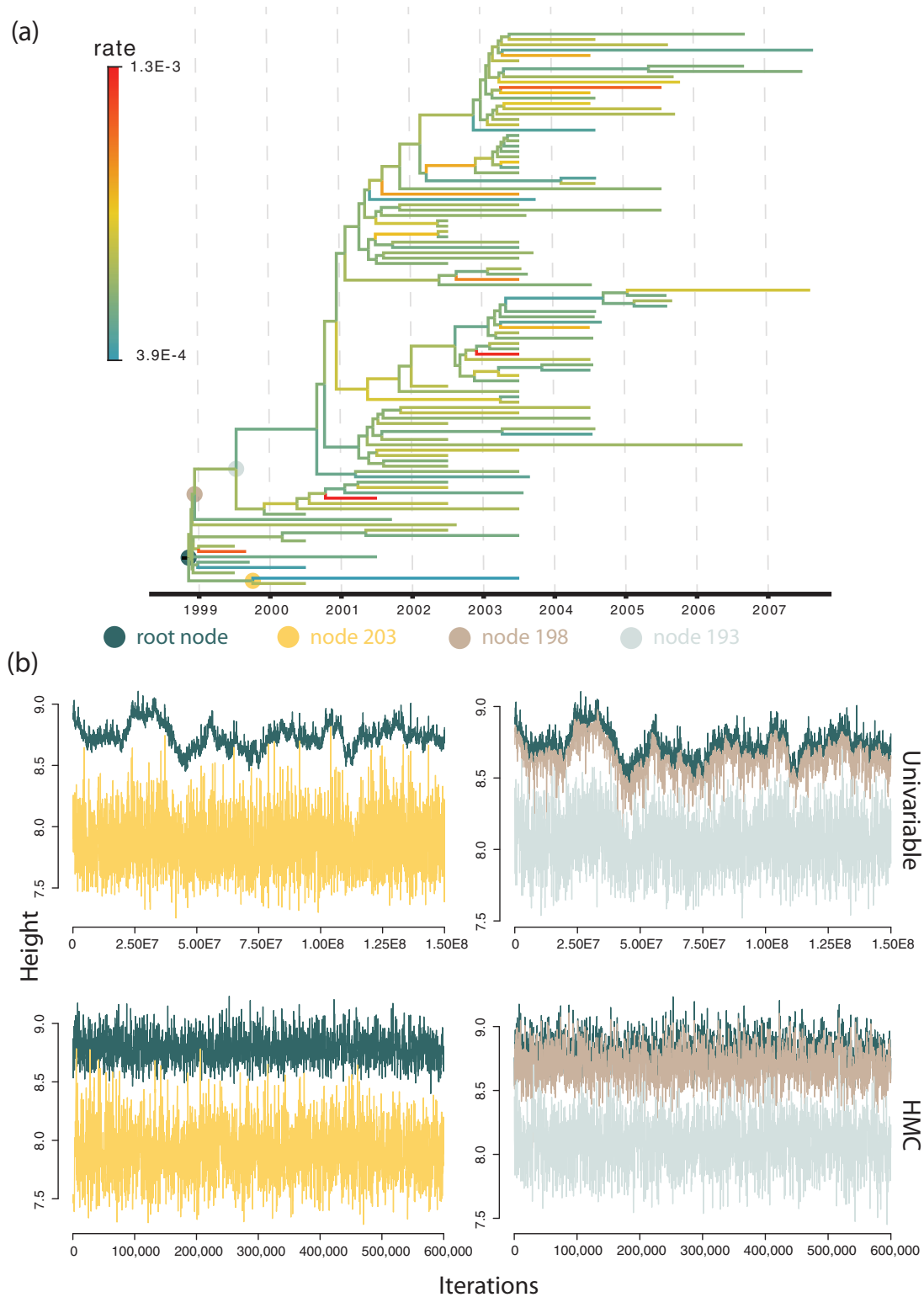


FIGURE 3. Trace plot of 4 height parameters indicated on the WNV phylogeny. a) The WNV phylogeny explored in the example. Branches are color-coded by the posterior means of the branch-specific evolutionary rates. Four representative nodes indicated by colored dots illustrate mixing issues at nodes close to the root when learning the posterior distribution of their heights using the univariable samplers. b) The trace plots of the height parameter of the 4 nodes indicated in a) using the same color scheme. The top 2 trace plots are obtained with the univariable samplers for an MCMC chain of length 1.5×10^8 iterations. The bottom 2 trace plots are obtained with the HMC sampler for an MCMC chain of length 600,000. The trace of the root height is shown in both plots for the same sampler to compare with other nodes.

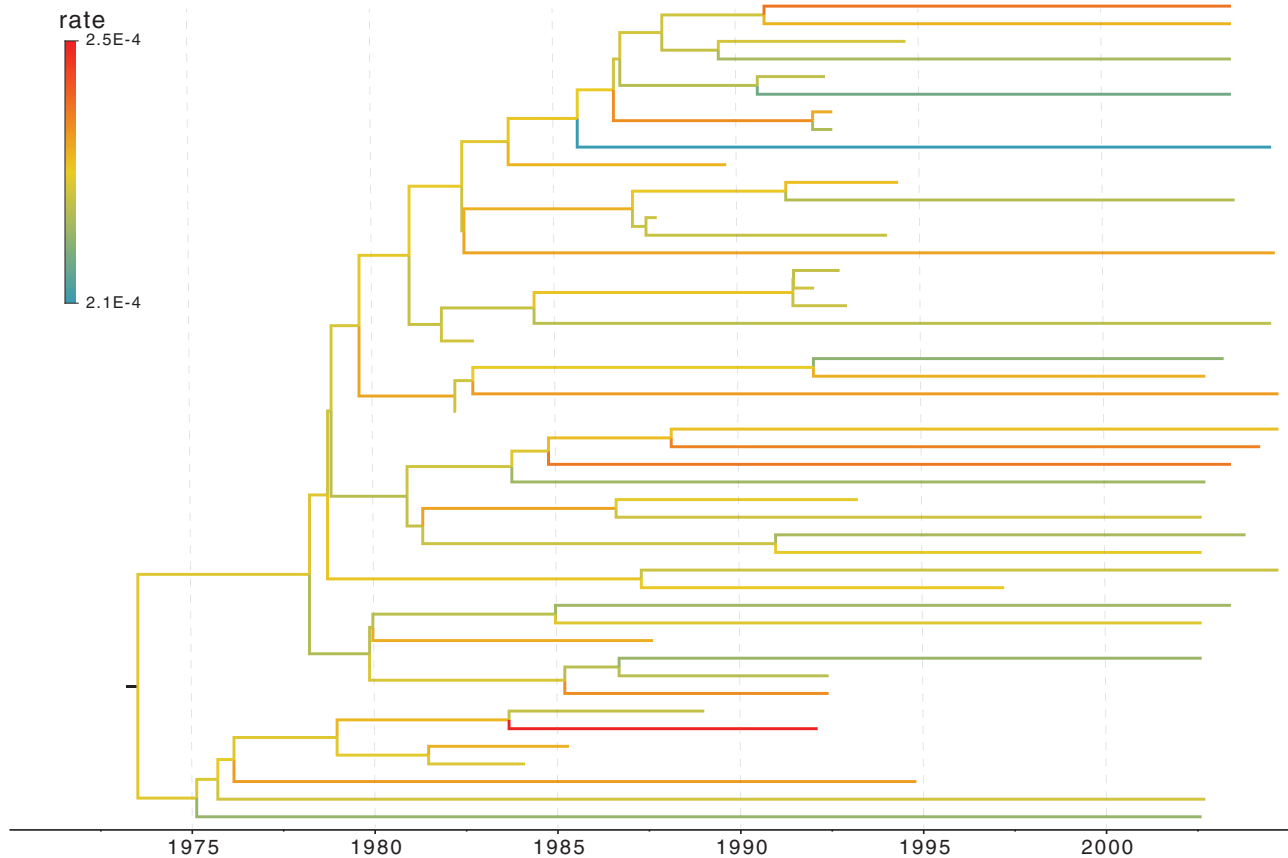


FIGURE 4. The RABV phylogeny explored in the example. Branches are color-coded by the posterior means of the branch-specific evolutionary rates.

an artifact, we ran three independent MCMC chains with the same model and confirmed that they converged to the same posterior distribution. Our estimated date of the MRCA of the MAN14985 clade (Fig. 6b III) is 2019.49 (2019.42, 2019.54) and the estimated date of the MRCA of the KAT21596 set (Fig. 6b IV) is 2018.96 (2018.83, 2019.07).

Algae Our analysis yields a posterior mean rate $5.35 (4.97, 5.73) \times 10^{-3}$ substitutions per site per million years. The scale parameter has posterior mean 0.60 (0.52, 0.69). Figure 7 shows the maximum clade credible evolutionary tree of the algae example. The date of the root of the tree is inferred to be 194.0 (163.8, 229.3) Mya. This is slightly older than the estimate in Pena et al. (2020) and our 95% Bayesian credible interval is wider.

DISCUSSION

The confounding of evolutionary rate and time has imparted divergence time estimation with high uncertainty and low reliability of the inference. Nonetheless, much effort and improvement have shaped the molecular clock models to better characterize evolutionary rate

heterogeneity along phylogenies (Thorne et al. 1998; Kishino et al. 2001; Drummond et al. 2006; Rannala and Yang 2007; Lemey et al. 2010; Lartillot et al. 2016; Bletsa et al. 2019). We here introduce a linear-time transformation of the internal node height parameters into a ratio space with the aim to improve estimation efficiency under complex molecular clock models. Naive transformation of the gradient of the log-likelihood from the original height space into the ratio space results in $\mathcal{O}(N^2)$ computations. To make the transformation scalable, we present linear-time algorithms that improve the performance of this transformation. With a slight modification, Algorithm 4 builds upon Algorithm 2 to calculate all derivatives of the log-determinant of the Jacobian matrix also in linear-time. This collection of linear-time algorithms enables researchers to employ dynamic-based samplers (e.g., HMC) to sample the internal node heights and substantially improve inference.

When applying HMC on all dimensions in the ratio space, the sampler proposes a new set of values for the height parameter and all ratios that corresponds to a set of new values for all internal node heights in the original height space. Alternatively, one may cycle HMC on subsets of dimensions from the ratio space in

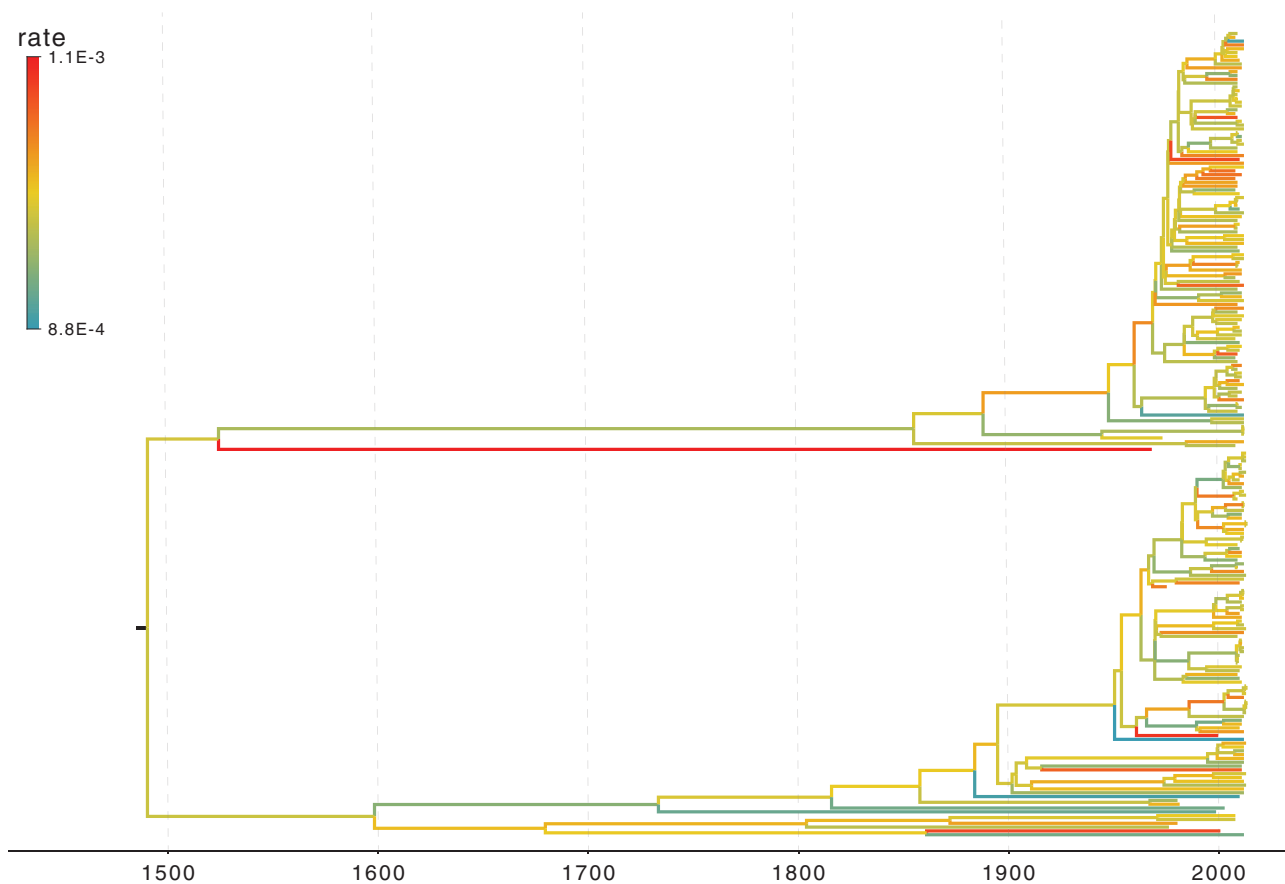


FIGURE 5. The LASV phylogeny explored in the example. Branches are color-coded by the posterior means of the branch-specific evolutionary rates.

a Metropolis-within-Gibbs inference strategy such that in each iteration, HMC proposes new values to only a subset of dimensions. For example, one possible choice of these subsets is to separately sample the root height and all the ratios (i.e., one subset containing only the height parameter and one subset containing all ratio parameters). Interestingly, each of the two subsets takes a full traversal for updating the gradient through Algorithms 2 and 3 where the postorder traversal updates the gradient with respect to all ratio parameters ($N - 2$ dimensional) and the preorder traversal updates only the height parameter (single dimensional). Therefore, sometimes it might be more computationally efficient to mix the classic univariable sampling kernels with HMC for the height dimension to benefit from the low computational load for learning the root height dimension. For example, one may apply classic univariable samplers on the height dimension in ratio space instead of HMC. In addition, one may apply classic univariable samplers on the original root height dimension such that with careful caching of the previous iteration, each proposal only needs updating 2 postorder partial likelihood vectors corresponding to the 2 immediate descendant branches from the root. However, as illustrated by the WNV

example, classic univariable samplers may suffer from the constraints on the node heights resulting in poor mixing in some dimensions (e.g., several internal nodes close to the root in this case), where the mixture of samplers may lead to worse computational efficiency. To investigate the univariable sampler's validity, we ran the chain $10\times$ longer for the WNV example. As expected, the trace plot of the longer chain exhibits a normal "caterpillar" shape that indicates both the validity and limitation of the univariable samplers. Interestingly, in other examples where we do not observe MCMC mixing issues for the univariable sampler, the HMC sampler still outperforms the univariable sampler as shown in Figure 2 and Table 1 by generating higher ESS per unit time for the dimension with the minimum ESS (for which one usually waits to grow larger than certain threshold before terminating the MCMC chain). The sampling efficiency is more uniform across dimensions in the HMC sampler as compared to the univariable sampler. This more uniform performance across different dimensions is partly because our adaptive variance informed mass matrix \mathbf{M} accounts for different levels of variability among dimensions. For example, Ji et al. (2020) show a better performance of an HMC sampler with a mass

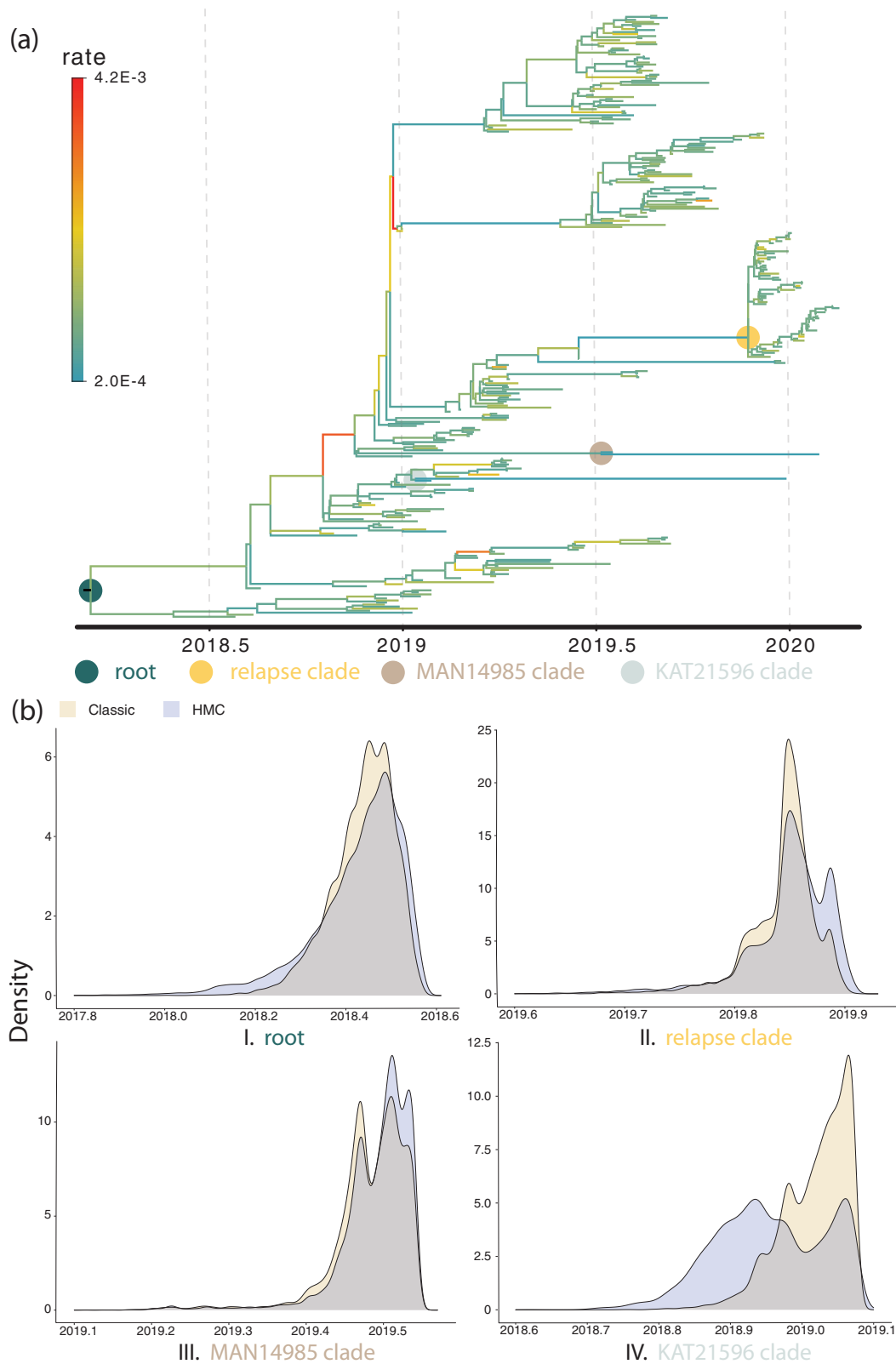


FIGURE 6. Kernel density estimation plot of the tMRCA distribution of 4 clades of interest on the EBOV phylogeny. a) The EBOV phylogeny explored in the example. Branches are color-coded by the posterior means of the branch-specific evolutionary rates. We use 4 colored dots to indicate the 4 MRCA nodes of 4 clades of interest. b) The kernel density estimation plot of the tMRCA of the 4 nodes indicated in a).

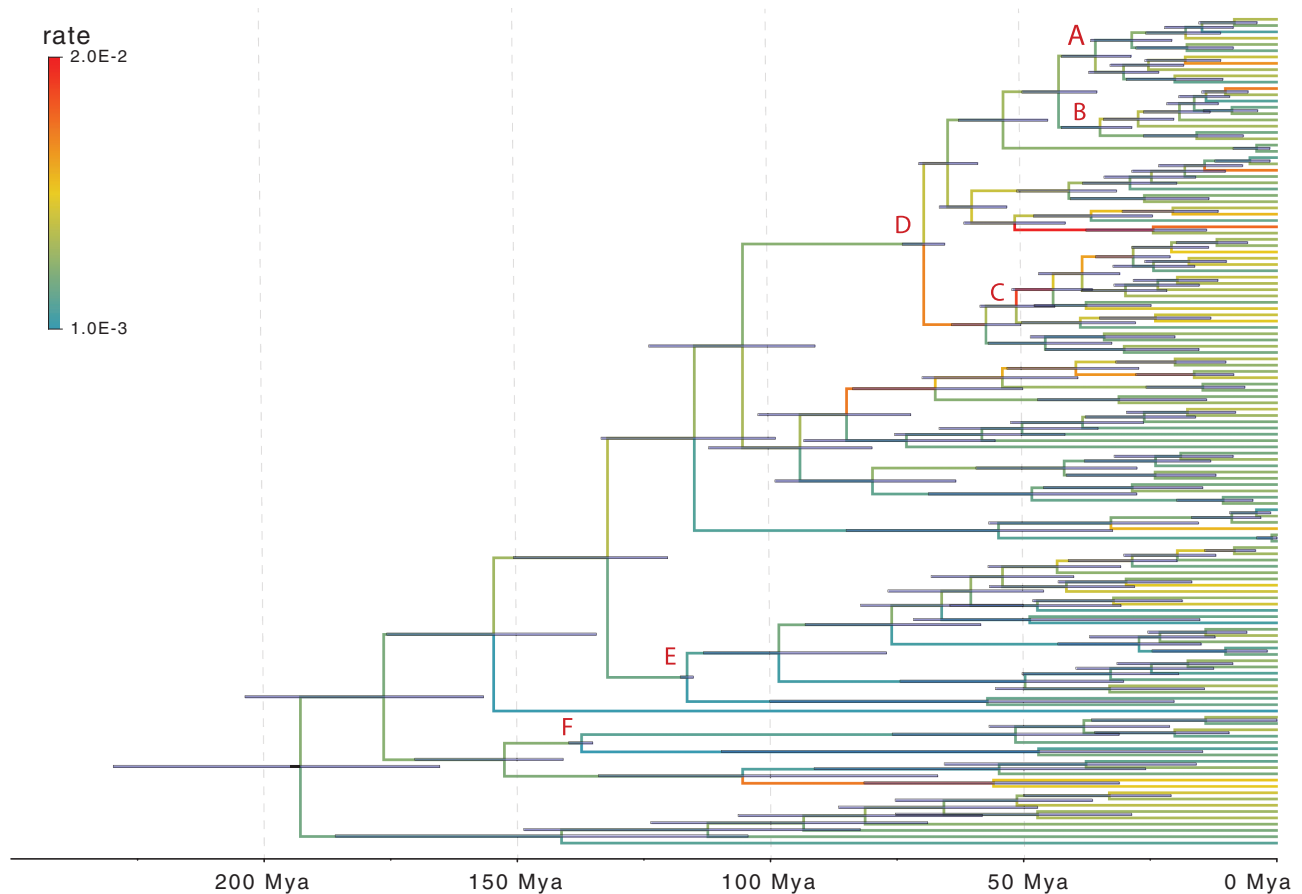


FIGURE 7. The algae phylogeny explored in the example. Branches are color-coded by the posterior means of the branch-specific evolutionary rates. Horizontal bars represent 95% posterior credible intervals for the internal node times. Letters a)–f) indicate where fossil record informed calibration normal priors are placed on the tMRCAs of clade a: *Harveyolithon*, clade b: *Porolithon*, clade c: *Lithophyllum pustulatum*, clade d: Hydrolithoideae, clade e: Hapalidiales, and clade f: Sporolithales.

matrix informed by the diagonal of the Hessian matrix as compared to a vanilla HMC sampler with a mass matrix composed of an identity matrix. Another possible cause is that we do not tune separate univariable samplers for dimensions with different levels of variability where one may propose smaller jumps for dimensions with small variations and larger jumps for dimensions with large variations. However, Fisher et al. (2021) show that allowing each dimension to tune a separate univariable sampler results in little improvement as compared to HMC. The mass matrix employed in this study has only diagonal entries being non-zero that is equivalent to rescaling the dimensions by their variability. Such a rescaling method has already shown its success in divergence time estimations (e.g., such as in Thorne et al. (1998) and Rannala and Yang (2003)).

The EBOV example employs a more general mixed-effects relaxed clock model with clade-specific fixed-effects and branch-specific random-effects. The original study (Mbala-Kingebeni et al. 2021) incorporates rate variation into a strict molecular clock model by introducing a single parameter to capture fixed-effects

from the clades of interest. Their molecular clock model therefore has 2 dimensions. The mixed-effects model employed in this study now utilizes a 597-dimensional parameter (4 dimensions for clade-specific fixed-effects with an intercept term, 592 dimensions for branch-specific random-effects, and 1 dimension for the scale parameter) to capture multiple sources of rate variation. This more general mixed-effects model detects the same slow-down of the evolutionary rate of the branch leading to the relapse clade. Interestingly, the relapse clade and the MAN14985 clade are monophyletic with posterior probability approaching 1 in our analyses whereas the KAT21596 clade is monophyletic with posterior probability 0.37 compared to the posterior probability of 0.95 in the original study. The lower posterior probability estimate for the 2 sequences (KAT21596 and BTB4325) forming a monophyletic clade indicates a different mixture of tree topologies partly owing to the more general molecular clock model and potentially better mixing of node heights in each topology. The difference in posterior probability of the KAT21596 clade further affects the multi-modal

posterior distribution of tMRCAs of the two sequences as in [Figure 6b](#). While our approach reveals clearer multimodal distributions, it remains an important research direction to study its performance in revealing multimodalities and possibly improving mixing efficiency over tree topologies through more intense investigations (e.g., through simulation studies) which, however, is out of the scope of this manuscript.

The algae example also employs a more general mixed-effects relaxed clock model with clade-specific fixed-effects and branch-specific random effects that expands the dimension of the molecular clock-related parameter from 9 (1 dimension for base-line molecular clock rate and 8 dimensions for fix-effects from clades of interest) to 272 (9 dimensions for clade-specific fixed-effects with an intercept term, 262 dimensions for branch-specific random-effects, and 1 dimension for the scale parameter) to capture additional sources of rate variation. As shown in [Figure 7](#), our analysis reveals substantial within-clade rate variation that was not modeled previously and a slightly different topology of the maximum clade credible evolutionary tree (e.g., the placement of clade C: *L. pustulatum*). The large variation in the branch-specific evolutionary rates may also contribute to the wider posterior credible interval estimated for the root time and the tMRCAs of several clades. As demonstrated in their study on the effect of molecular clock rate model choices ([dos Reis et al. 2018](#)), it is important for future studies to explore such influence on divergence time estimations with fossil calibration priors under now computationally feasible branch-specific evolutionary rate models.

Recent molecular clock models add additional dependence of evolutionary rate onto time ([Aiewsakun and Katzourakis 2015](#); [Ho et al. 2015](#); [Membrebe et al. 2019](#)) that bring in more biological insights into the time-dependency of the evolutionary rates in viral evolution. However, such a dependence structure further complicates the confounding of evolutionary rate and time. Fortunately, the complex dependence structure only affects the derivatives without influencing the ratio transformation or the HMC machinery and is, therefore, the reason Equation (6) uses more general terms $\partial b_i / \partial t_i$, $\partial b_j / \partial t_i$, and $\partial b_k / \partial t_i$.

A caveat of the linear-time algorithms that are introduced here is that they assume sampling dates are given and fixed. Often, viral sequences are associated with various levels of uncertainty, not only in their associated metadata (e.g., sampling dates) but also with regard to sequencing quality. Typically, a quality control step removes unreliable sequences. In addition, fossil records with sequence information may present as ancient tip nodes with associated uncertainties. In a Bayesian framework, one may integrate out sampling date uncertainty through their support so that sampling dates become parameters of the model and are no longer fixed ([Pybus et al. 2012](#)). The proposed algorithms and HMC machinery remain unaffected if one cycles between sampling all internal node heights

and tip heights from their full conditional distributions. However, the derivative with respect to the height parameter in the ratio space needs to consider contributions from the tip nodes when one samples all node heights (including variable tip heights) jointly. Moreover, the anchor node and epoch constructions become variable and need to be jointly updated with tip heights. Another caveat of our algorithms is that we do not formally consider degree-2 internal nodes such as those employed in a “total-evidence” dating analysis (see, e.g., [Stadler \(2010\)](#) and [Gavryushkina et al. \(2014\)](#)) although one may effectively transform them into regular degree-3 nodes by adding length-zero branches to these degree-2 nodes connected with a tip node with sequences (if any) switched from the original degree-2 internal nodes. In addition, some models may introduce discontinuity or non-smoothness into the target density, such as the “soft-bound” calibration priors introduced in [Yang and Rannala \(2006\)](#) that are continuous over the parameter space but that have derivatives with respect to node heights that do not exist for a finite number of points. Although the rejection step in the Metropolis–Hastings algorithm corrects any bias caused by the discontinuity or non-smoothness such that HMC still samples from the correct target density, these issues may increase the numerical integration error in the leap-frog step and thereby reduce sampling efficiency. Fortunately, the pioneering work of [Nishimura et al. \(2020\)](#) has demonstrated a promising HMC variant to solve issues generated by discontinuities. All these remain important avenues of future work.

ACKNOWLEDGMENTS

We thank the 3 anonymous reviewers and the editors for their thoughtful comments that significantly improve the quality of this manuscript.

FUNDING

The research leading to these results has received funding from the European Research Council under the European Union’s Horizon 2020 research and innovation programme (grant agreement no. 725422—ReservoirDOCS). The Artic Network receives funding from the Wellcome Trust through project 206298/Z/17/Z. M.A.S. and X.J. are partially supported by NIH grants U19 AI135995, R56 AI149004, R01 AI153044, and R01 AI162611. X.J. acknowledges support from the NVIDIA academic hardware grant program. G.B. acknowledges support from the Interne Fondsen KU Leuven / Internal Funds KU Leuven under grant agreement C14/18/094 and from the Research Foundation—Flanders (‘Fonds voor Wetenschappelijk Onderzoek—Vlaanderen’, G0E1420N and G098321N). P.L. acknowledges support by the Research Foundation—Flanders (‘Fonds voor Wetenschappelijk Onderzoek—Vlaanderen’, G066215N,

G0D5117N, and G0B9317N). J.L.T. was supported by NSF DEB 1754142.

CONFLICT OF INTEREST

The authors declare no conflicts of interest.

SUPPLEMENTARY MATERIAL

Data available from the Dryad Digital Repository: <http://dx.doi.org/10.5061/dryad.n02v6wx21>.

REFERENCES

- Aiewsakun P., Katourakis A. 2015. Time dependency of foamy virus evolutionary rate estimates. *BMC Evol. Biol.* 15(1):1–15.
- Andersen K.G., Shapiro B.J., Matranga C.B., Sealfon R., Lin A.E., Moses L.M., Folarin O.A., Goba A., Odiya I., Ehiane P.E., Momoh M., England E.M., Winnicki S., Branco L.M., Gire S.K., Phelan E., Tariyal R., Tewhey R., Omoniwa O., Fullah M., Fonnies R., Fonnies M., Kanneh L., Jalloh S., Gbakie M., Saffa S., Karbo K., Gladden A.D., Qu J., Stremlau M., Nekoui M., Finucane H.K., Tabrizi S., Vitti J.J., Birren B., Fitzgerald M., McCowan C., Ireland A., Berlin A.M., Bochicchio J., Tazon-Vega B., Lennon N.J., Ryan E.M., Bjornson Z., Milner D.A., Lukens A.K., Brodie N., Rowland M., Heinrich M., Akdag M., Schieffelin J.S., Levy D., Akpan H., Bausch D.G., Rubins K., McCormick J.B., Lander E.S., Günther S., Hensley L., Okogbenin S., Schaffner S.F., Okokhere P.O., Khan S.H., Grant D.S., Akpede G.O., Asogun D.A., Gnrirke A., Levin J.Z., Happi C.T., Garry R.F., Sabeti P.C. 2015. Clinical sequencing uncovers origins and evolution of Lassa virus. *Cell* 162(4): 738–750.
- Andrieu C., De Freitas N., Doucet A., Jordan M.I. 2003. An introduction to MCMC for machine learning. *Machine Learn.* 50(1–2): 5–43.
- Andrieu C., Thoms J. 2008. A tutorial on adaptive MCMC. *Stat. Comput.* 18(4): 343–373.
- Ayres D.L., Cummings M.P., Baele G., Darling A.E., Lewis P.O., Swofford, D.L., Huelsenbeck, J.P., Lemey, P., Rambaut, A., Suchard, M.A. 2019. Beagle 3: improved performance, scaling, and usability for a high-performance computing library for statistical phylogenetics. *Syst. Biol.* 68(6): 1052–1061.
- Baele G., Gill M.S., Lemey P., Suchard M.A. 2020. Hamiltonian Monte Carlo sampling to estimate past population dynamics using the skygrid coalescent model in a Bayesian phylogenetics framework. *Wellcome Open Res.* 5(53): 53.
- Baele G., Lemey P., Rambaut A., Suchard M.A. 2017. Adaptive MCMC in Bayesian phylogenetics: an application to analyzing partitioned data in BEAST. *Bioinformatics* 33(12): 1798–1805.
- Biek R., Henderson J.C., Waller L.A., Rupprecht C.E., Real L.A. 2007. A high-resolution genetic signature of demographic and spatial expansion in epizootic rabies virus. *Proc. Natl. Acad. Sci USA* 104(19): 7993–7998.
- Bletsa M., Suchard M.A., Ji X., Gryseels S., Vrancken B., Baele G., Worobey M., Lemey, P. 2019. Divergence dating using mixed effects clock modelling: an application to HIV-1. *Virus Evol.* 5(2): vez036.
- Casella G., Berger R.L. 2001. *Statistical inference*. 2nd ed. Pacific Grove, CA: Duxbury.
- Dinh V., Bilge A., Zhang C., Matsen IV F.A. Probabilistic path Hamiltonian Monte Carlo. *Proceedings of the 34th International Conference on Machine Learning—Volume 7; 2017; pp. 1009–1018. JMLR.org.*
- dos Reis M., Gunnel G.F., Barba-Montoya J., Wilkins A., Yang Z., Yoder A.D. 2018. Using phylogenomic data to explore the effects of relaxed clocks and calibration strategies on divergence time estimation: primates as a test case. *Syst. Biol.* 67(4): 594–615.
- Drummond A.J., Ho S.Y., Phillips M.J., Rambaut A. 2006. Relaxed phylogenetics and dating with confidence. *PLoS Biol.* 4(5): e88.
- Düx A., Lequime S., Patrono L.V., Vrancken B., Boral S., Gogarten J.F., Hilbig A., Horst D., Merkel K., Prepoint B., Santibanez S., Schlotterbeck J., Suchard M.A., Ulrich M., Widulin N., Mankertz A., Leendertz F.H., Harper K., Schnalke T., Lemey P., Calvignac-Spencer S. 2020. Measles virus and rinderpest virus divergence dated to the sixth century BCE. *Science* 368(6497): 1367–1370. doi: 10.1126/science.aba9411.
- Erwin D.H., Laflamme M., M. Tweedt S., Sperling E.A., Pisani D., Peterson, K.J. 2011. The cambrian conundrum: early divergence and later ecological success in the early history of animals. *Science* 334(6059): 1091–1097.
- Fisher A.A., Ji X., Zhang Z., Lemey P., Suchard M.A. 2021. Relaxed random walks at scale. *Syst. Biol.* 70(2): 258–267.
- Fourment M., Darling A.E. 2019. Evaluating probabilistic programming and fast variational Bayesian inference in phylogenetics. *PeerJ* 7: e8272.
- Gavryushkina A., Welch D., Stadler T., Drummond A.J. 2014. Bayesian inference of sampled ancestor trees for epidemiology and fossil calibration. *PLoS Comput. Biol.* 10(12): e1003919.
- Gill M. S., Lemey P., Bennett S.N., Biek R., Suchard M.A. 2016. Understanding past population dynamics: Bayesian coalescent-based modeling with covariates. *Syst. Biol.* 65(6): 1041–1056.
- Haario H., Saksman E., Tamminen J. 1999. Adaptive proposal distribution for random walk Metropolis algorithm. *Comput. Stat.* 14(3): 375–396.
- Hadfield J., Brito A.F., Swetnam D.M., Vogels C.B., Tokarz R.E., Andersen K.G., Smith R.C., Bedford T., Grubaugh N.D. 2019. Twenty years of West Nile virus spread and evolution in the Americas visualized by Nextstrain. *PLoS Pathog.* 15(10): e1008042.
- Hassler, G.W., Magee, A.F., Zhang, Z., Baele, G., Lemey, P., Ji, X., Fourment, M. and Suchard, M.A., 2023. Data Integration in Bayesian Phylogenetics. *Ann. Rev. Stat. Appl.* 10: 353–377.
- Hastings W.K. 1970. Monte Carlo sampling methods using Markov chains and their applications. *Biometrika* 57(1): 97–109.
- Ho S.Y., Duchêne S., Molak M., Shapiro B. 2015. Time-dependent estimates of molecular evolutionary rates: evidence and causes. *Mol. Ecol.* 24(24): 6007–6012.
- Ji X., Zhang Z., Holbrook A., Nishimura A., Baele G., Rambaut A., Lemey P., Suchard M.A. 2020. Gradients do grow on trees: a linear-time $O(N)$ -dimensional gradient for statistical phylogenetics. *Mol. Biol. Evol.* 37(10): 3047–3060.
- Kishino H., Thorne J.L., Bruno W.J. 2001. Performance of a divergence time estimation method under a probabilistic model of rate evolution. *Mol. Biol. Evol.* 18(3): 352–361.
- Lartillot N., Phillips M.J., Ronquist F. 2016. A mixed relaxed clock model. *Phil. Trans. Royal Soc. B: Biol. Sci.* 371(1699): 20150132.
- Lemey, P., Hong, S.L., Hill, V., Baele, G., Poletto, C., Colizza, V., O’toole, Á., McCrone, J.T., Andersen, K.G., Worobey, M., Nelson M.I., Rambaut A., Suchard M.A. 2020. Accommodating individual travel history and unsampled diversity in Bayesian phylogeographic inference of SARS-CoV-2. *Nat. Commun.* 11(1): 5110.
- Lemey P., Rambaut A., Welch J.J., Suchard M.A. 2010. Phylogeography takes a relaxed random walk in continuous space and time. *Mol. Biol. Evol.* 27(8): 1877–1885.
- Mbala-Kingebeni P., Pratt C., Mutafali-Ruffin M., Pauthner M.G., Bile F., Nkuba-Ndaye A., Black A., Kinganda-Lusamaki E., Faye J., Aziza A., Diagne M.M., Mukadi D., White B., Hadfield J., Gangavarapu K., Bisento N., Kazadi D., Nsunda B., Akonga M., Tshiani O., Misasi J., Ploquin A., Epaso V., Sana-Paka E., N’kassar Y.T.T., Mambu F., Edidi F., Matondo M., Bula Bula J., Diallo B., Keita M., Belizaire M.R.D., Fall I.S., Yam A., Mulangu S., Rimion A.W., Salfati E., Torkamani A., Suchard M.A., Crozier I., Hensley L., Rambaut A., Faye O., Sall A., Sullivan N.J., Bedford T., Andersen K.G., Wiley M.R., Ahuka-Mundeke S., Muyembe Tamfum J.-J., 2021. Ebola Virus transmission Initiated by relapse of systemic Ebola virus disease. *N. Engl. J. Med.* 384(13): 1240–1247. doi: 10.1056/NEJMoa2024670.

- Membrebe J.V., Suchard M.A., Rambaut A., Baele G., Lemey P. 2019. Bayesian inference of evolutionary histories under time-dependent substitution rates. *Mol. Biol. Evol.* 36(8): 1793–1803.
- Meredith R.W., Janečka J.E., Gatesy J., Ryder O.A., Fisher C.A., Teeling E.C., Goodbla A., Eizirik E., Simão T.L., Stadler T., Rabosky D.L., Honeycutt R.L., Flynn J.J., Ingram C.M., Steiner C., Williams T.L., Robinson T.J., Burk-Herrick A., Westerman M., Ayoub N.A., Springer M.S., Murphy W.J. 2011. Impacts of the cretaceous terrestrial revolution and KPg extinction on mammal diversification. *Science* 334(6055): 521–524. doi: 10.1126/science.1211028.
- Metropolis N., Rosenbluth A.W., Rosenbluth M.N., Teller A.H., Teller E. 1953. Equation of state calculations by fast computing machines. *J. Chem. Phys.* 21(6): 1087–1092.
- Neal R.M. 2011. MCMC using Hamiltonian dynamics. *Handbook of Markov Chain Monte Carlo* 2(11).
- Nishimura A., Dunson D.B., Lu J. 2020. Discontinuous hamiltonian monte carlo for discrete parameters and discontinuous likelihoods. *Biometrika* 107(2): 365–380.
- Pena V., Vieira C., Braga J.C., Aguirre J., Rösler A., Baele G., De Clerck O., Le Gall L. 2020. Radiation of the coralline red algae (corallinophycidae, rhodophyta) crown group as inferred from a multi-locus time-calibrated phylogeny. *Mol. Phylogenet. Evol.* 150, 106845.
- Pybus O.G., Suchard M.A., Lemey P., Bernardin F.J., Rambaut A., Crawford F.W., Gray R.R., Arinaminpathy N., Stramer S.L., Busch M.P., Delwart E.L. 2012. Unifying the spatial epidemiology and molecular evolution of emerging epidemics. *Proc. Natl. Acad. Sci. USA* 109(37): 15066–15071. doi: 10.1073/pnas.1206598109.
- Rannala B., Yang Z. 2003. Bayes estimation of species divergence times and ancestral population sizes using DNA sequences from multiple loci. *Genetics* 164(4): 1645–1656.
- Rannala B., Yang Z. 2007. Inferring speciation times under an episodic molecular clock. *Syst. Biol.* 56(3): 453–466.
- Roberts G.O., Rosenthal J.S. 2009. Examples of adaptive MCMC. *J. Computat. Graph. Stat.* 18(2): 349–367.
- Salvatier J., Wiecki T.V., Fonnesbeck C. 2016. Probabilistic programming in Python using PyMC3. *PeerJ Comput. Sci.*
- Simion P., Delsuc F., Philippe H. 2020. To what extent current limits of phylogenomics can be overcome? Scornavacca, Celine; Delsuc, Frédéric; Galtier, Nicolas. *Phylogenetics in the Genomic Era*, No commercial publisher | Authors open access book, pp.2.1:1–2.1:34.
- Stadler T. 2010. Sampling-through-time in birth–death trees. *J. Theor. Biol.* 267(3): 396–404.
- Stan Development Team (2017). *Stan modeling language users guide and reference manual*, Version 2.17.0.
- Suchard M.A., Lemey P., Baele G., Ayres D.L., Drummond A.J., Rambaut A. 2018. Bayesian phylogenetic and phylodynamic data integration using beast 1.10. *Virus Evol.* 4(1): vey016.
- Thorne J.L., Kishino H., Painter I.S. 1998. Estimating the rate of evolution of the rate of molecular evolution. *Mol. Biol. Evol.* 15(12): 1647–1657.
- Tierney L. 1994. Markov chains for exploring posterior distributions. *Ann. Stat.*, 1701–1728.
- World Health Organization. 2021. Ebola outbreak 2018-2020- north kivu/ituri, drc. Available from: <https://www.who.int/emergencies/situations/Ebola-2019-drc->.
- Yang Z., Rannala B. 2006. Bayesian estimation of species divergence times under a molecular clock using multiple fossil calibrations with soft bounds. *Mol. Biol. Evol.* 23(1): 212–226.
- Zuckermandl E., Pauling L.B. 1962. Molecular disease, evolution and genic heterogeneity. In Kasha M., Pullman B., editors. *Horizons in biochemistry*. New York, NY: Academic Press. p. 189–225.